Dual-Reject-Band Filters With Resonant Apertures in Rectangular Waveguide

Joaquin F. Valencia Sullca, Santiago Cogollos, *Member, IEEE,* Vicente E. Boria, *Fellow, IEEE,*
Marco Guglielmi, *Life Fellow, IEEE,* Simone Bastioli, *Senior Member, IEEE*
and Richard Snyder, *Life Fellow, IEEE*

***Abstract*—This paper describes a new family of dual-reject-band filters in rectangular waveguide that uses resonant apertures, and is suitable for narrow-band applications. Reject-band filters are commonly used to protect from interference in both communication and earth observation systems. The filter structure that we propose is based on a simple modification of the traditional narrow-band reject-band filter. We first describe the basic dual-reject-band filter structure, then we discuss the results of a detailed parametric analysis (all relevant data are provided in the Appendix) to be used as a basis for the filter design procedure. The design of several dual-reject-band filter prototypes is discussed in detail, including sensitivity to manufacturing errors and high-power analysis. Finally, simulations and measurements are also compared, showing very good agreement, thereby fully validating both the design procedure and the new filter topology that we propose.**

***Index Terms*—Dual-reject-band, narrow-band, pass-band, reject-band filter, resonant apertures and wide-band.**

I. Introduction

BROAD-BAND receiving systems require the rejection of undesired local high power signals with minimal effect on the rest of the receiver pass-band. As a consequence, reject-band filters are normally used before low-noise amplifiers. Fig. 1 shows the block diagram of how a dual-reject-band filter can be used in broad-band receivers. When the presence of a high-power interference is detected, the dual-reject-band filter is inserted in the system using the single-pole, double throw switches (SPDT). When no high-power interference is present, the bypass is used instead. In this context, many different technologies can be used to implement microwave reject-band filters [1], [2], [3], [4], [5], and many examples implemented with planar technology can indeed be found in the technical literature [6], [7], [8], [9], [10], [11], [12], [13], [14], [15], [16]. However, common problems for all of the planar structures described in the literature is high insertion loss, limited rejection in the stopband, and low power handling capabilities.

This work has been supported by Ministerio de Ciencia, Innovación y Universidades (Spanish Government) through the R&D Projects PID2022-136590OB-C41 (under grant AEI/10.13039/501100011033/FEDER, UE) and TED2021-129196B-C41 (under grant 10.13039/501100011033/Unión Europea NextGenerationEU/PRTR). This paper is an expanded version from the IEEE MTT-S International Microwave Symposium (IMS 2023), San Diego, CA, USA, June 11-16, 2023. *(Corresponding author: Joaquin F. Valencia Sullca.)*

J.F. Valencia Sullca, S. Cogollos, V.E. Boria and M. Guglielmi, are with the Departamento de Comunicaciones, iTEAM Group, Universitat Politècnica de València, E-46022 Valencia, Spain (e-mails: joavasu2@teleco.upv.es, sancobo@dcom.upv.es, vboria@dcom.upv.es, marco.guglielmi@iteam.upv.es).

Simone Bastioli and Richard V. Snyder are with RS Microwave Company Inc., 10 Park Place, Butler, 07405 NJ, United States (e-mails: sbastioli@rsmicro.com, rsnyder@rsmicro.com).

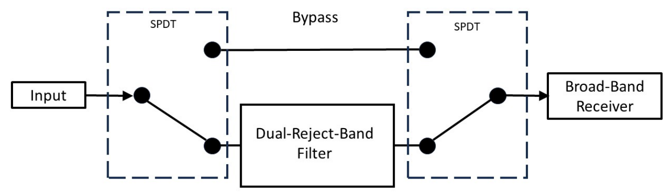

Fig. 1. Using a dual-reject-band filter in a broadband receiver.

On the other hand, reject-band microwave filters implemented in rectangular waveguide technology typically have low insertion loss and high power handling capabilities. In the remainder of this paper we will, therefore, focus only on rectangular waveguide structures.

The most classic implementation of a reject-band filter in rectangular waveguide is discussed in [3]. Furthermore, in [17], the design procedure for equal-element stop-band filters has been proposed for large (as well as for small) degrees of dissipation, and for any number of resonators. The design of magnetically tunable stop-band filters using ferromagnetic garnet resonators has also been proposed in [18].

In [19], a magnetically tunable stop-band filter in rectangular waveguide has been proposed. Also, compact, dual-mode absorptive reject-band cavity filters have been proposed in [20], with the objective of obtaining both minimum phase and elliptic responses. Furthermore, a new procedure for designing stop-band waveguide filters has been described in [21] and [22], showing how elliptic reject-band filters can be easily implemented. In [23], a stop-band filter has been designed using rectangular resonators coupled to the center dielectric strip of a non-radiative dielectric waveguide.

Moreover, further implementations have been proposed for the design of rectangular waveguide band-stop filter structures using E- or H-plane T-junctions loaded by rectangular irises [24]. Additional contributions describe a new approach for the synthesis of stop-band filters based on the use of multimode resonators [25] and [26]. In [27], a non-traditional approach is discussed for the synthesis of waveguide rejection cells using a dielectric rectangular post. In [28] and [29], dual-rejection-band filters have been implemented, where the structures are built combining dielectric resonators and microstrip resonators. In [30], waveguide reject-band filters based on partial height cylindrical metallic posts have been proposed. Furthermore, in [31] a novel in-line microwave reject-band and pass-band elliptic and pseudo-elliptic filters have been designed, using an offset partial-height post in a rectangular waveguide. Also, in [32] a simple rectangular waveguide section with two rectangular posts inside is shown to provide a frequency response with two rejection resonances. More recently in [33], a novel dual-band stop-band filter based on suspended stripline with short-ended waveguide stubs has been proposed.

Additionally in [34], a structure has been proposed using irises formed by slotted capacitive strips to implement simple notch filters. Also, in [35] stop-band and pass-band filters have been designed using stepped conductors, or stepped slots in irises. Furthermore, in [36] a stop-band filter structure is discussed, that consists of a rectangular cavity fed by a coupling slot milled on the broad wall of a rectangular waveguide. Also, in [37] a new composite left-right handed structure has been implemented with dielectrics and metal patches.

Recently, the design of a novel multi-band filters has been described in [38] and [39], where pass-band and stop-band waveguide filters have been obtained. Also, in [40], a novel miniaturized E-plane multiband stop-band waveguide filter has been implemented.

An additional possibility to implement pass-band or stop-band filter structures is offered by resonant apertures (RAs). In [41], for instance, multi-aperture irises in a rectangular waveguide have been used to build waveguide pass-band or stop-band filters. Additionally, a new approach for the design and implementation of microwave filters with single and dual stop-band is proposed in [42]. Also, in [43] in-line pseudo-elliptic reject-band filters with non-resonating nodes (NRNs) and/or phase shift sections are discussed. Furthermore, in [44], a compact E-plane waveguide filter structure has been designed, to couple band-reject cavities to the main rectangular waveguide in in-line band-stop filters.

More recently, a contribution has shown preliminary results on how to design dual-reject-band filters in rectangular waveguide based on the use of RAs with a very simple modification of the classic narrow-band reject-band filter structure [45].

In this context, therefore, the objective of this paper is to significantly extend the results presented in [45]. In particular, the additional new topics discussed with respect to our previous work are as follows:

1) A parametric analysis of the basic unit cell of the dual-band-reject filter has been added in Appendix, with the objective of demonstrating how the frequency location of both the first and second transmission zero (TZs), and of the return loss zero (RZ), can be controlled.
2) The development of an equivalent circuit model, in order to support the computation of the initial physical dimensions of the dual-reject-band filter.
3) Two systematic design procedures. One based on direct optimization, the other on the use of the equivalent circuit just developed.
4) A sensitivity analysis of the filter structures to investigate the sensitivity to manufacturing errors.
5) The high-power analysis of the hardware, in order to identify the power level at which multipaction is initiated. The results are also compared with the ones obtained with a standard single-reject-band filter.
6) The calculation of the unloaded Q in the dual-reject-band filters, as compared with the one obtained with a standard single-reject-band filter.

In the remainder of this paper, two separate dual-reject-band structures are discussed. The first structure that we discuss is a narrow dual-reject-band RA filter that provides two narrow band regions of rejection within a pass-band covering from 3.25 to 4.25 GHz, where each rejection band region is at least 53 MHz wide, and the value of the rejection is greater than 60 dB in the rejection bands. The target insertion loss in the pass-bands regions of this structure is less than 1 dB. The preliminary performance of this filter has already been discussed in [45], however, in this publication, additional details are provided.

The second structure that we discuss is a wider dual-reject-band RA filter that provides two regions of rejection with three pass-bands within a wider pass-band, covering from 2.75 to 4.50 GHz, where each reject-band region is significantly wider than the first example (95 MHz instead of 53 MHz), and where the value of the rejection is greater than 50 dB in the rejection bands. Furthermore, the return loss level of the three bandpass regions is now more than 20 dB. Although it is generally true that reject band filters tend to be narrow-band, we have explored also a wider reject band structure because, since the basic unit cell is novel, we have found it important to explore the limits of what can be achieved in terms of wider rejection bands.

Finally, in addition to theory, measured results are also discussed, showing excellent agreement with simulations, thereby fully validating both the new filter topologies and the design procedures that we propose.

II. Parametric Analysis of the Basic Unit Cell

In this section, we outline the results of the parametric analysis of the unit cell of the dual-reject-band (UCDRB) filter shown in Fig.2. The full set of results is reported in the Appendix. Fig. 3 shows the simulated response of the structure in Fig. 2 (from [45]). The unit cell can produce two TZs and a RZ between the TZs.

The physical explanation of the behavior of this simple structure is as follows [45]:

- To start, the dimensions of both the resonant aperture and the vertical rectangular waveguide stub are independently chosen so that they resonate at the same frequency.
- The vertical stub is then connected in parallel to the RA to form the basic unit-cell.

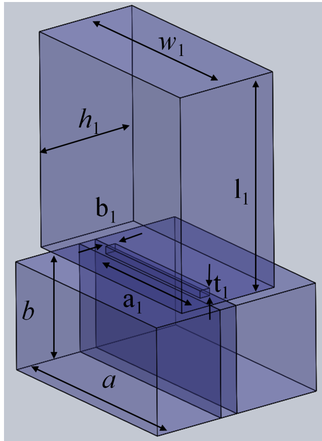

Fig. 2. Structure of the unit cell of the dual-reject-band filter [45].

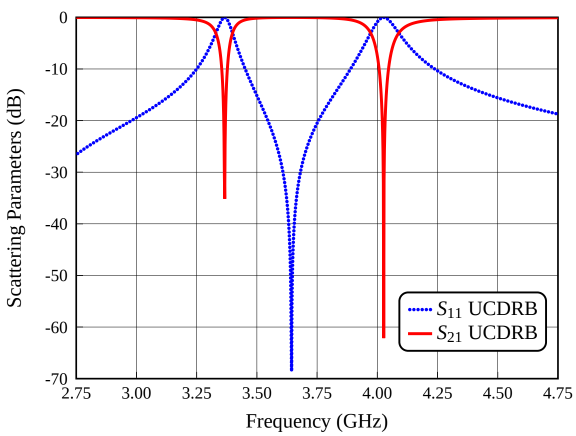

Fig. 3. Simulated performance of the unit cell of the dual-reject-band filter.

- At the resonant frequency, the vertical waveguide stub has zero input impedance. As a consequence, the RA is short-circuited, and the RZ is produced.
- At frequencies that are lower than the frequency of the RZ, the vertical stub has a negative (capacitive) reactance. As a consequence, the resonant frequency of the RA is lowered, and the first TZ is generated.
- At frequencies higher than the RZ, the vertical stub has a positive (inductive) reactance. As a consequence, the resonant frequency of the RA is increased, and the second TZ is generated.

The performance shown in Fig. 3 has been obtained with the commercial tool FEST3D (v.2023 by AuroraSAT, now with Dassault Systèmes).

The parametric analysis is a necessary step in order to better understand the relation between the various structural parameters, and the performance of the basic unit cell. In this context, we have chosen the standard waveguide WR-229 ($a = 58.166$ mm and $b = 29.083$ mm). The typical operating frequency band for this waveguide is from 3.3 to 4.9 GHz.

The parameters that we have investigated are:

- The width a_1 of the RA.
- The height b_1 of the RA.
- The width w_1 of the resonator.
- The length l_1 of the resonator.
- The width h_1 of the resonator.
- The thickness t_1 of the RA.

From the results of the parametric analysis that we have carried out (see the Appendix for the detailed data), it is evident that, strictly speaking, we do not have completely independent control over the three features of the basic unit cell (namely, the frequency location of TZ1, RZ, and TZ2). However, our finding clearly indicate that, using optimization, some modicum of independent control is indeed possible, so that we do have the possibility of allocating the position of TZ1, RZ, and TZ2 according to our needs.

III. Narrow Reject-Band Design

We first describe the design procedure for the dual-reject-band filter with narrow rejection bands.

It is important to mention, at this point, that the implementation and simulation of the narrow dual-reject-band RA filter has already been discussed in detail in [45]. However, for the sake of completeness, we will include in this paper only a brief outline. The procedure we have used is as follows:

1) We first design a unit cell of the dual-reject-band filter with two TZs (f_1 and f_3) and one RZ (f_2) at frequency locations that are consistent with the required specifications. This step can be done manually since the waveguide structure (see Fig. 2) is very simple, and consequently, the simulation time in low accuracy is very small.
2) Next, we connect two identical unit-cells with a standard waveguide section of length $L \approx \lambda/4$, at the frequency of the RZ (f_2).
3) We then add additional unit cells to the structure in order to obtain the desired rejection bandwidths and levels.
4) Finally, we optimize the dimensions a_i, b_i of the RAs, and w_i and l_i of the vertical resonators, and the separation between unit-cells L_i. The optimization process is very rapid, since the structure is still very simple and the simulation is carried out in low accuracy.

This procedure is very effective for narrow reject-band structures. If we need to design a structure with wider rejection bandwidths, we need a more structured approach, as described in the next section. Another important point is that the result presented in this section has been obtained with a low accuracy setting (of the employed full-wave simulation tool cited before, i.e. FEST3D). The transition from low accuracy to high accuracy (either using FEST3D or any other advanced software tool, such as CST Studio Suite) will be discussed in a later section of this paper.

IV. Wide Reject-Band Design

To design structures with wider rejection bands, it is more convenient to build first an equivalent circuit (or model), and to introduce a number of changes in the basic unit cell. These changes are needed in order to provide additional degrees of freedom for the final optimization of the filter performance. In this context, a mixed lumped-distributed model has been

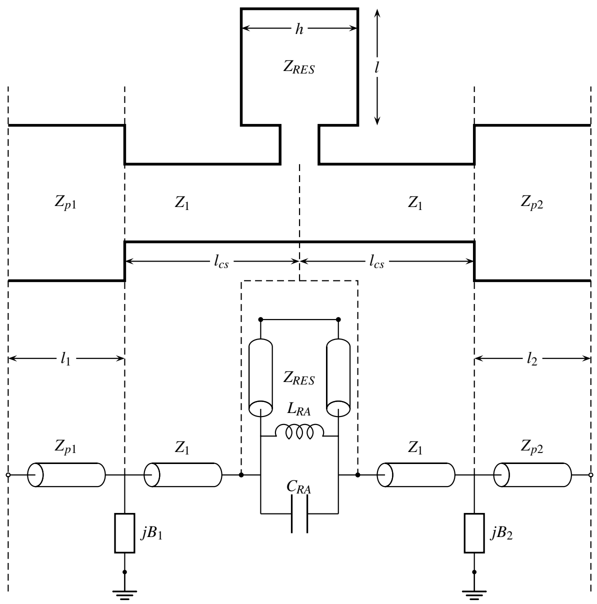

Fig. 4. Unit cell (E-plane cut) and its equivalent circuit.

found to be more convenient. The basic unit cell and its corresponding model are shown in Fig. 4. The susceptances B_1 and B_2 are not free parameters. Their values are obtained from [46] (Formula 2a page 307) using the formulas for the equivalent model of a change in height in a rectangular waveguide. The actual independent parameters are, in fact, the changes in heights in the waveguide model. The RA in the upper port of the T-junction is modeled with the parallel resonator L_{RA} and C_{RA}. The remaining elements are transmission lines representing the fundamental mode of the corresponding waveguide. Fig. 5 shows the model of the complete filter. Cascading modified unit cells leads to the geometry shown in Fig. 6.

A. Unit Cell Design

To start, let us assume that we know the parameters of the model in Fig. 4, namely, we assume that we know the following parameters :

- The input/output waveguide sections: impedances Z_{p1}, Z_{p2} and corresponding lengths l_1 and l_2.
- The lines connected to the junction. They are symmetrical and therefore we have two parameters: line impedance Z_1 and its length l_{cs}.
- The circuit elements representing the RA: L_{RA}, C_{RA}.
- The resonator parameters: line impedance Z_{RES} and its length l.

It is important to note that in the above parameters, there are, in fact, only two parameters that need to be known, namely, the width and the height of the relevant waveguide cross section. In the mainline of the structure, however, we have kept the width of the waveguides (a of the standard waveguide) constant, and the height is optimized (one variable per impedance). With this choice, the steps between lines are capacitive (not resonant). However, when resonators Z_{RES} are optimized there is also the freedom to choose the width w and height h simultaneously (two variables per impedance).

The relation between the geometry of the modified waveguide unit cell and the elements of the model is as follows:

1) The capacitive steps at the input/output of the modified waveguide unit cell are represented in the lumped element model by the shunt susceptances B_1 and B_2.
2) Between the capacitive step and the junction, we have a length l_{cs} of uniform rectangular waveguide with characteristic impedance Z_1 of width $a_{cs} = a$ and height b_{cs}. In general, the characteristic impedance of every transmission line in the model is computed using the following expression (power-voltage definition):

$$Z_C = 2\frac{b}{a}Z_{\text{TE}} \tag{1}$$

where Z_{TE} is the frequency-dependent modal impedance of the fundamental mode. A similar procedure has also been used in [47]. The initial values of the three parameters are set as follows: $a_{cs} = a$ (not optimized), $b_{cs} = b$ and $l_{cs} > 0$. The later value (for l_{cs}) with the additional objective of avoiding a strong interaction near the junction and, at the same time, simplifying the fabrication.
3) Next, the shunt combination of capacitor C_{RA} and inductor L_{RA} is used to model the RA. The relevant geometrical parameters are the width a_{RA}, height b_{RA} and thickness t of the resonant aperture (a_1, b_1 and t_1 in Fig. 2). The values of these parameters are obtained from the resonant frequency of the aperture f_0, and from the susceptance slope parameter $\mathcal{B}$ using the following relationships:

$$f_0 = \frac{1}{2\pi\sqrt{L_{RA}C_{RA}}} \tag{2a}$$

$$\mathcal{B} = \sqrt{\frac{C_{RA}}{L_{RA}}} \tag{2b}$$

It is, therefore, irrelevant if we work in the circuit model with L_{RA} and C_{RA} or f_0 and $\mathcal{B}$. We assume that we have their values, and we have to obtain the physical parameters of the RA from the circuit model. The first step is to build an E-plane T-Junction (see Fig. 7) in an EM simulator (FEST3D in this case) with the two mainline ports ((1) and (2) in Fig. 7) with the dimensions given by Z_1 (obtained in the previous step using $a_{cs} = a$ and b_{cs}). The third port (waveguide with dimensions w and h of the resonator cross-section) is attached to the RA with dimensions a_{RA}, b_{RA} set to an initial value obtained from the needed resonant frequency. The resonator length is irrelevant now because we are placing a port instead a short-circuited resonator. This is very convenient, since the scattering parameters do not change their module if the reference planes of the ports are moved. This is represented in Fig. 7 with dotted lines placed at the ports. The thickness t is fixed to a convenient value for mechanical reasons ($t = 2$ mm in this case). Next, a_{RA} and b_{RA} are optimized until the scattering parameters

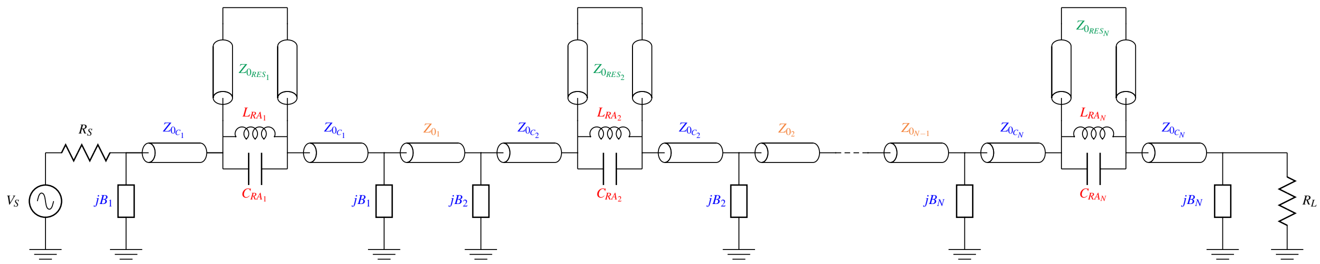

Fig. 5. Lumped-distributed model of the dual-reject-band filter.

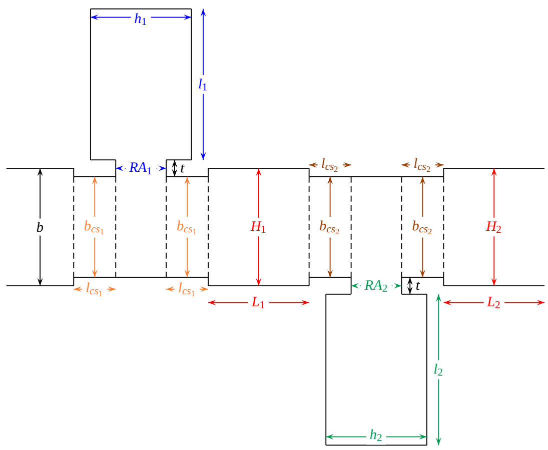

Fig. 6. Modified waveguide unit cells cascaded to obtain the EM model of the dual-reject-band filter with wider rejection bands. This EM model is the physical equivalent of the equivalent circuit (model) shown in Fig. 5.

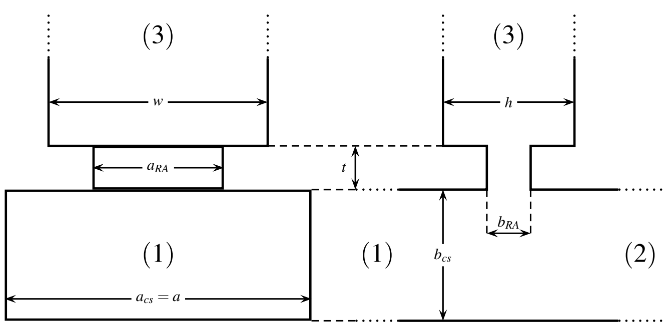

Fig. 7. E-plane T-junction front view (left) and side view (right). Ports are numbered within parenthesis.

(S_{11}, S_{21} and S_{31}) of the EM model match those of the circuit model. This optimization is very fast, since only two variables are involved, namely, a_{RA} and b_{RA}.

4) With the line of impedance Z_{RES} in Fig. 4 connected to the shunt resonator (representing the RA), it is now possible to design the vertical resonator connected to the top of the RA with width w, height h and length l.
5) The lines with impedance Z_{0_i} in Fig. 5 allow the connection of the unit cells of the dual-reject-band filter. Since they are transmission lines, their waveguide equivalents are obtained directly, together with the rest of the lines of the circuit model.

B. Design of the Dual-Reject-Band Filter at Circuit Level

This step is carried out optimizing the model shown in Fig. 5. Of course, we need a good initial point to start the optimization. Let us assume that the filter specifications are given in form of two reject bands of BW_1 and BW_2 each with center frequencies f_1 and f_2, respectively. The algorithm to establish the circuit model with an initial guess is as follows:

1) The first step is to find the location of the TZs required to achieve the equiripple behavior within these bands. As a good approximation, the zeros of the N-th Chebyshev polynomial in the lowpass domain are used:

$$\Omega_{TZ_k} = \cos\left[\frac{(2k-1)\pi}{2N}\right] \quad \forall k = 1, \ldots, N \tag{3}$$

The zeros are then moved to the reject bands using the typical lowpass to bandpass transformation. Therefore

$$\Omega_{TZ_k} = \frac{f_1}{BW_1}\left(\frac{f_{1TZ_k}}{f_1} - \frac{f_1}{f_{1TZ_k}}\right) \quad \forall k = 1, \ldots, N \tag{4a}$$

$$\Omega_{TZ_k} = \frac{f_2}{BW_2}\left(\frac{f_{2TZ_k}}{f_2} - \frac{f_2}{f_{2TZ_k}}\right) \quad \forall k = 1, \ldots, N \tag{4b}$$

Solving then equations (4) for f_{1TZ_k} and f_{2TZ_k}, we obtain the values of the TZs for the first and second band, respectively.

2) Once the initial guess of the TZs is established, we select the TZs in pairs. Each par will contain a TZ of each band. Each pair will be assigned to each unit cell capable of producing two TZs (one per band).
3) The frequency of the RZ of each cell is selected at the center frequency of the pass-band. Note that this RZ is enforced by the line Z_{RES} (see Fig. 4) at the frequency when the line is exactly $\lambda_g/2$ in length.
4) The center frequency and slope parameter of the RA in (2) are selected to achieve the TZs at the frequencies that we have selected for each cell in step 2). It is important now to recall the parametric analysis carried out in section II, because the real structure allows only

TABLE I
VALUES FOR THE ELEMENTS OF THE MODEL IN FIG. 5

		Cell 1	Cell 2	Cell 3	Cell 4	Cell 5
In/Out cell lines	b_{cs} (mm)	28.076	30.225	29.733	34.572	29.389
	l_{cs} (mm)	12.130	9.961	10.941	9.660	15.814
Resonant Apertures	L_{RA} (nH)	2.990	8.052	12.390	6.964	2.936
	C_{RA} (pF)	0.717	0.275	0.175	0.314	0.694
Stubs	l (mm)	72.144	85.579	95.814	83.661	72.907
	h (mm)	26.707	20.917	25.898	24.622	35.432
	a (mm)	52.885	48.192	47.002	47.498	51.721
Inter-cell lines	H (mm)	29.083	29.083	29.083	29.083	
	L (mm)	11.634	15.740	17.619	11.814	

limited values in the frequencies of the TZs (i.e. the slope parameter and center frequency of the RA).

5) Once each individual cell is designed, all cells are cascaded to obtain the circuit shown in Fig. 5. The frequency of the TZs are preserved when the cells are cascaded but the RZs interact with each other. Therefore, at this point an optimization procedure at circuit level, is required to obtain an equiripple behavior within the rejection and transmission bands. This procedure is very fast since the model is very simple. During the optimization, the limits found in the parametric analysis are used to avoid an unrealistic solution during this stage. Table I gives the values that we have obtained for the model in Fig. 5.
6) Finally, when the model of the whole filter fulfills the specifications, the circuit is disassembled cell by cell. Each unit cell element is related to the real structure equivalent using the procedure described in section IV-A. Following this procedure, the physical structure of the filter is ready to be assembled, thus obtaining the initial point for the EM design stage. After few steps of optimization, the final EM structure is easily obtained.

C. Wide Band Dual-Reject-Band Filter Design Example

To validate our design procedure, we propose to design a wide dual-reject-band RA filter with three pass-bands between the rejection bands. Table II shows the specification of the filter. Fig. 8 shows the response of the wide dual-reject-band RA filter obtained from the lumped-distributed circuit (AWR), together with the initial waveguide (FEST3D) model (see Fig. 5 and 6), respectively. As we can see, the performance of initial waveguide model is reasonably close to the response of the ideal lumped-distributed circuit. Fig. 9 shows the response of the wide dual-reject-band RA filter obtained from the lumped-distributed circuit (AWR), together with the final waveguide (FEST3D) model, after optimization. Fig. 10 shows the geometry of the structure.

As we can see from Fig. 9, the agreement between the performance obtained with the lumped-distributed model, and the one obtained with the waveguide model, is very good. We can now obtain a rejection level greater than 50 dB in the two rejection bands. The rejection bandwidths are now 95 MHz

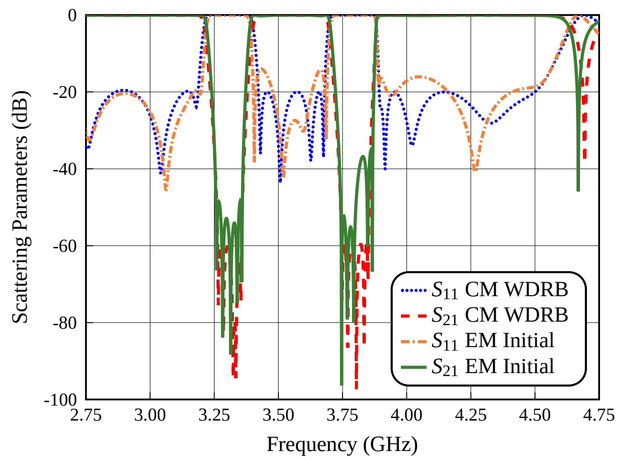

Fig. 8. Simulated performance of the lumped-distributed circuit (CM WDRB), and initial waveguide model (WM) of the five-pole wide dual-reject-band RA filter, using AWR Design Environment and FEST3D, respectively.

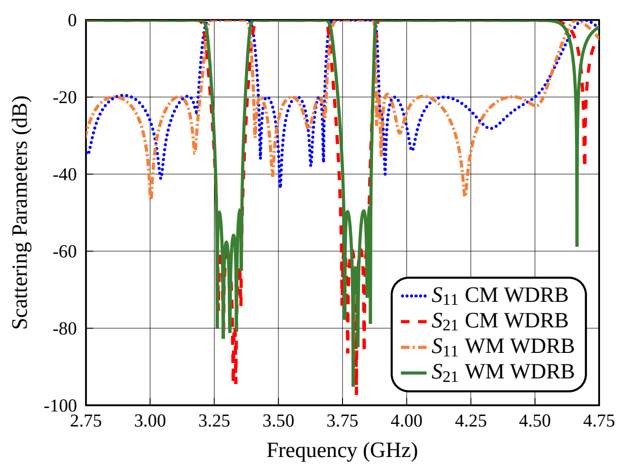

Fig. 9. Simulated performance of the lumped-distributed circuit (CM WDRB), and optimized waveguide model (WM) of the five-pole wide dual-reject-band RA filter, using AWR Design Environment and FEST3D, respectively.

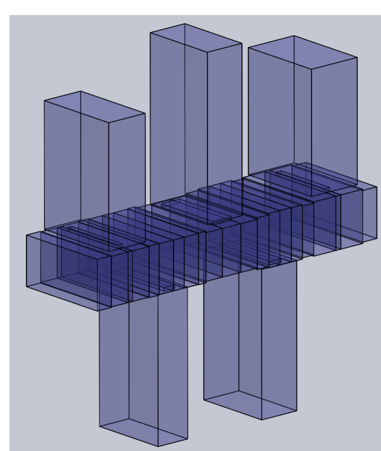

Fig. 10. Structure of the five-pole wide dual-reject-band RA filter with E-plane T-Junctions.

(lower) and 102.5 MHz (upper) wide. The return loss levels achieved in the three pass-bands is better than 20 dB.

V. High Accuracy Narrow Dual-Reject-Band Prototype

The narrow dual-reject-band filter structure that we have designed so far, has been simulated with the commercial tool FEST3D in the low accuracy (LA) mode. However, we now need to go from the LA to the HA (High Accuracy) simulation space. The transition from the LA to the HA space has been carried out following the same procedure described in [45], namely, a combination of [48] and the well-known aggressive space mapping (ASM) procedure [49].

As a verification before manufacturing, we have also simulated the same structure with the full-wave electromagnetic simulator FEST3D in the high accuracy mode, including in the HA simulations up to 120 accessible modes, 360 basis functions, and 3600 terms for computing the Green's function [50].

To continue, we now note that the narrow dual-reject-band RA filter structure has already been described in detail in [45], where we have shown the final structure with rounded corners in the vertical resonators, and we have given a table with the final values for all the dimensions. For the sake of space, we have, therefore, not duplicated in this paper the same information.

VI. High Accuracy Wide Dual-Reject-Band Prototype

Next, we discuss the wide dual-reject-band RA filter structure (see Fig. 11). The transition from the LA space to the HA space has been carried out following the same procedure already discussed for the narrow band case.

The specifications for the wide-band structure are given in Table II. Also in this case, we have replaced the concave corners of the vertical resonators with rounded corners with a radius equal to $r_1 = 3$ mm, and all concave corners of the capacitive steps with a radius equal to $r_2 = 1$ mm.

The final structure that we have obtained is shown in Fig. 11. Fig. 12 shows the comparison of the simulated performances obtained with FEST3D and CST Studio Suite (v.2023, CST GmbH, now with Dassault Systèmes). As we can see, the agreement is very good. Table III shows the final values for all structural dimensions. The thickness of the RAs is t_i, and all the vertical resonators have the same width as the input waveguide.

VII. Measurements

The dual-reject-band filter prototypes discussed in Sections V and VI have been manufactured in a clam shell configuration, using a standard computer numerical control (CNC) milling process. It is important to mention that to obtain the measurement results, we have used the standard waveguide calibrations for the WR-229, with the TRL (Through, Reflection and Line) method. Additionally, the noise floor of the calibration was about -70 dB.

TABLE II
Electrical specifications for the wide dual-reject-band RA filter

	Parameter	Requirement
Lower rejection band	Center frequency	3.31 GHz
	Rejection level	> 50 dB
	Rejection bandwidth	95 MHz
Upper rejection band	Center frequency	3.81 GHz
	Rejection level	> 50 dB
	Rejection bandwidth	102.5 MHz
Lower pass-band	Center frequency	2.95 GHz
	In-band return loss	> 20 dB
	Bandwidth	490 MHz
Center pass-band	Center frequency	3.545 GHz
	In-band return loss	> 20 dB
	Bandwidth	280 MHz
Upper pass-band	Center frequency	4.2 GHz
	In-band return loss	> 20 dB
	Bandwidth	636 MHz

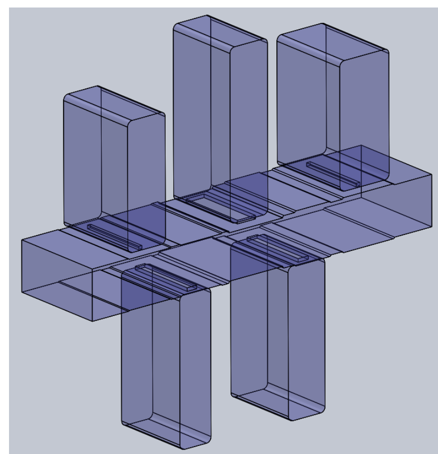

Fig. 11. Structure of the wide dual-reject-band RA filter designed with radius equal to $r_1 = 3$ mm in the vertical resonators, and all the capacitive steps with a radius equal to $r_2 = 1$ mm.

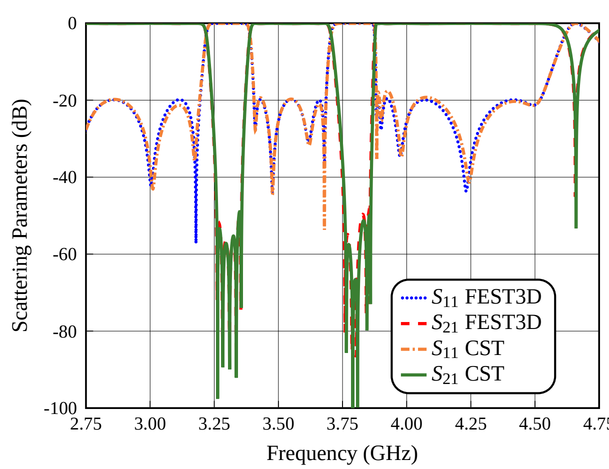

Fig. 12. Simulated performance of the wide dual-reject-band RA filter using FEST3D and CST Studio Suite.

TABLE III
PHYSICAL DIMENSIONS FOR THE WIDE DUAL-REJECT-BAND RA FILTER

Section Type	Dimensions (all in mm)	
Input Waveguide	a =58.17 b =29.083 $L_{input} = L_{output}$ =25	
Resonant aperture 1-5	a_1 =42.377 b_1 =2.078 t_1 =2.000	a_5 =41.003 b_5 =2.493 t_5 =2.000
Capacitive Steps 1-5	a_{cs_1} =58.170 b_{cs_1} =28.447 l_{cs_1} =12.789	a_{cs_5} =58.170 b_{cs_5} =30.480 l_{cs_5} =16.271
Resonator 1-5	w_1 =52.833 h_1 =25.304 l_1 =73.276	w_5 =51.866 h_5 =33.050 l_5 =72.456
Waveguide 1-4	W_1 =58.170 H_1 =29.083 L_1 =6.976	W_4 =58.170 H_4 =29.083 L_4 =7.781
Resonant aperture 2-4	a_2 =42.909 b_2 =6.384 t_2 =2.000	a_4 =42.156 b_4 =6.827 t_4 =2.000
Capacitive Steps 2-4	a_{cs_2} =58.170 b_{cs_2} =28.238 l_{cs_2} =10.398	a_{cs_4} =58.170 b_{cs_4} =30.539 l_{cs_4} =8.729
Resonator 2-4	w_2 =48.212 h_2 =20.886 l_2 =85.924	w_4 =47.458 h_4 =24.688 l_4 =85.821
Waveguide 2-3	W_2 =58.170 H_2 =29.083 L_2 =5.378	W_3 =58.170 H_3 =29.083 L_3 =8.102
Resonant aperture 3	a_3 =42.431 b_3 =12.043 t_3 =2.000	
Capacitive Step 3	a_{cs_3} =58.170 b_{cs_2} =26.841 l_{cs_2} =11.913	
Resonator 3	w_3 =46.877 h_3 =25.216 l_3 =97.690	

A. Narrow Dual-Reject-Band RA Filter

The narrow dual-reject-band RA filter prototype has been described in detail in [45], where we have shown the comparison between measured and simulated responses of the filter. The reader is therefore referred to [45].

B. Wide Dual-Reject-Band RA Filter

Next, we have manufactured the wide dual-reject-band RA filter, as shown in Fig. 13. The comparison between measured and simulated responses are shown in Fig. 14, 15 and 16.

As we can see, the pass-bands are centered at 2.95, 3.545 and 4.2 GHz, the reflection zeros are clearly visible, and the agreement with the simulation data is excellent. However, the RL of the third pass-band is slight degraded with respect to the simulations.

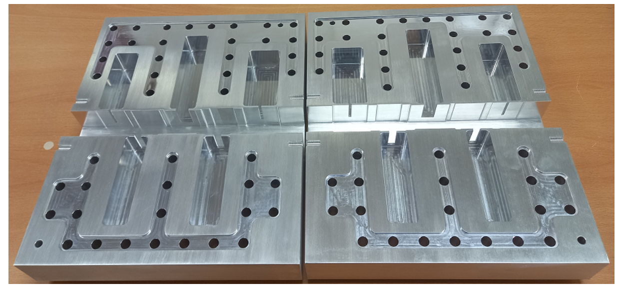

Fig. 13. Manufactured wide dual-reject-band RA prototype in two aluminum halves (no silver plating).

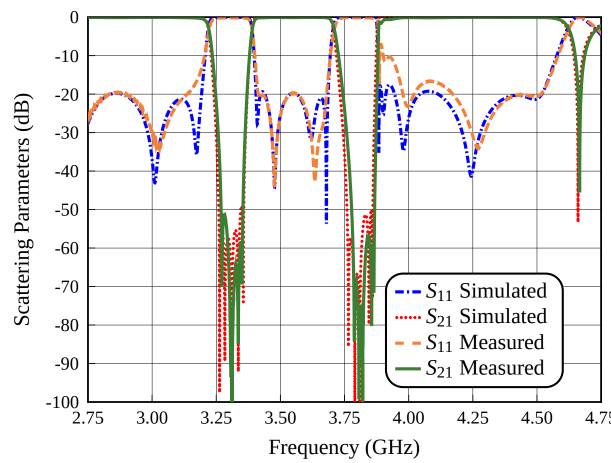

Fig. 14. Measurement of the performance of the wide dual-reject-band RA filter compared with the EM simulation (CST Studio Suite).

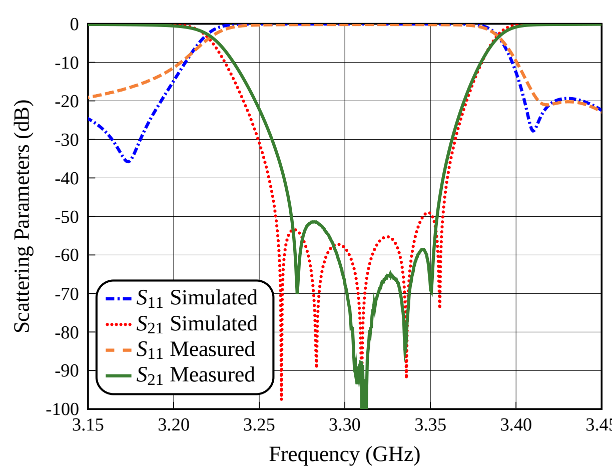

Fig. 15. Measurement of the performance of the wide dual-reject-band RA filter compared with the EM simulation (CST Studio Suite) for the lower rejection band.

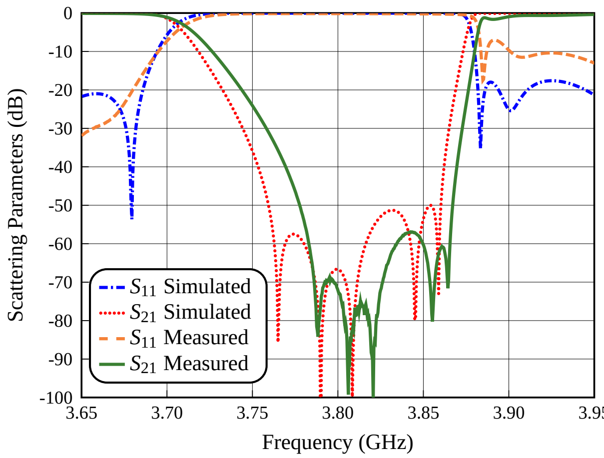

Fig. 16. Measurement of the performance of the wide dual-reject-band RA filter compared with the EM simulation (CST Studio Suite) for the upper rejection band.

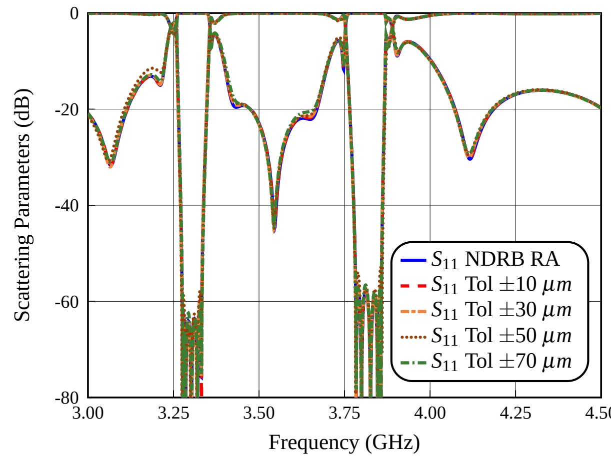

Fig. 17. Tolerance analysis of the narrow dual-reject-band RA filter.

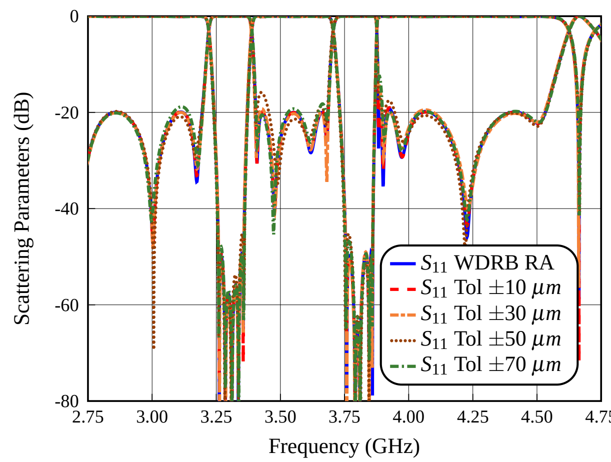

Fig. 18. Tolerance analysis of the wide dual-reject-band RA filter.

TABLE IV
RESULTS OF THE TOLERANCE ANALYSIS FOR THE NARROW AND WIDE DUAL-REJECT-BAND RA FILTERS

Filter Type	Yield of the Structure					
Tolerance	10 μm	20 μm	30 μm	40 μm	50 μm	70 μm
NDRB RA	100 %	97 %	91 %	76 %	56 %	35 %
WDRB RA	84 %	57 %	50 %	37 %	24 %	7 %

Furthermore, there is a slight disagreement between the simulations and the measurements in the out-of-band performance, namely, a small shift in the frequency of the rejection bands. Nevertheless, the agreement between the simulations and the measurements is good enough to validate both the filter structure and the proposed design procedure.

The discrepancies are fully justified by the limited accuracy of the manufacturing process (the manufacturing tolerance was estimated to be about 50 μm). This point has been confirmed with a sensitivity analysis, as detailed in Section VIII.

VIII. Yield Analysis

Next, we show the results of the yield analysis that we have carried out for both the narrow and the wide band filters. For this purpose, we have used the commercial tool FEST3D to introduce a random error with a Gaussian distribution in the filter dimensions.

The sensitivity analysis has been carried out with different values of the standard deviation, namely, $\pm$ 10, $\pm$ 20, $\pm$ 30, $\pm$ 40, $\pm$ 50 and $\pm$ 70 μm. Furthermore, since the pass-bands of the wide dual-reject-band RA filters have been designed with a return loss of 20 dB, the threshold value for the yield estimation has been set to 18 dB. Table IV shows a summary of the results obtained for the two dual-reject-band RA filters, where the starting letters N and W in the filter type indicate narrow and wide band, respectively.

Figs. 17 and 18 show a number of simulations, including random errors for the dual-reject-band RA filters.

As we can see from both the simulations and the results in Table IV, the narrow dual-reject-band RA filter (NDRB RA) is less sensitive to manufacturing errors in comparison with the wide dual-reject-band RA filter (WDRB RA). This fact is also reflected in the measured results that have been discussed in Section VII.

It is interesting to note, at this point, that the result we just obtained appears to be the exact opposite of what normally happens for pass-band filters in rectangular waveguide, namely, the wider the pass-band, the *lower* the sensitivity to manufacturing errors. For the reject-band discussed in this paper, the situation is reversed, namely, the wider the pass-band, the *higher* the sensitivity to manufacturing errors.

IX. High Power Analysis

In this section, we have identified the power (Watts) where the multipactor effect can be initiated in our filter structures. This is because the multipactor behavior of the filters is one of the most important features for space applications [51]. The multipactor simulations have been carried out using SPARK3D, with the SEY of aluminum (SEY=2.98), and

TABLE V
HIGH POWER ANALYSIS OF THE NARROW DUAL-REJECT-BAND RA FILTER

Structure	Power of the structure (in Watts)				
Frequency	RA_1	RA_2	RA_3	RA_4	RA_5
$f_1 = 3.258$ GHz	17.34	3.71	5.82	8.89	65.23
$f_2 = 3.357$ GHz	17.97	32.81	20.78	46.48	164.06
$f_3 = 3.550$ GHz	26079	62076	36158	21399	$> 10^6$
$f_4 = 3.751$ GHz	317	38.44	25.47	33.98	62.11
$f_5 = 3.872$ GHz	23.28	59.37	63.12	133.59	768.72

TABLE VI
HIGH POWER ANALYSIS OF THE WIDE DUAL-REJECT-BAND RA FILTER

Structure	Power of the structure (in Watts)				
Frequency	RA_1	RA_2	RA_3	RA_4	RA_5
$f_1 = 2.950$ GHz	1275	3875	6725	4950	1875
$f_2 = 3.221$ GHz	16.21	123	987	825	685
$f_3 = 3.387$ GHz	8699	375	362	175	99
$f_4 = 3.545$ GHz	10499	95196	115500	15250	75995
$f_5 = 3.703$ GHz	33.01	825	1485	4749	631
$f_6 = 3.875$ GHz	71.87	53.12	206	114	125
$f_7 = 4.200$ GHz	1900	10200	34350	10400	197

TABLE VII
HIGH POWER ANALYSIS OF THE FIRST STANDARD SINGLE-REJECT-BAND FILTER

Structure	Power of the structure (in Watts)				
Frequency	b_1	b_2	b_3	b_4	b_5
$f_1 = 3.252$ GHz	343.75	1312	3224	2171	14624
$f_2 = 3.343$ GHz	284.36	64.84	44.14	103.9	440.61

with the following set of parameters SEY0=0.5, E1(eV)=23.3, Emax(eV)=150.

Tables V and VI show the power thresholds that we have obtained for both the narrow and the wide dual-reject-band RA filters.

As expected, the resonant apertures (RA_2 and RA_1) show the lowest power threshold at 3.258 and 3.221 GHz, with 3.71 and 16.21 W for the narrow and the wide dual-reject-band RA filter, respectively.

To further evaluate the high power performance of both the narrow and wide dual-reject-band RA filters described in this contribution, we have computed the power thresholds of two standard single-reject-band filters (SRB Filter I and SRB Filter II), that have been designed at 3.3 and 3.31 GHz with a bandwidth of 53 and 95 MHz, and with 60 and 50 dB of rejection level, respectively. The power thresholds that we have obtained are shown in Table VII and VIII, respectively.

As expected, the capacitive window $b_3 = 6.471$ mm and $b_2 = 11.153$ mm of the two standard single-reject-band filters show the lowest power threshold values at 3.343 and 3.365 GHz with 44.14 and 192.18 W, respectively. This power level is indeed higher than the power level allowed by our narrow and wide dual-reject-band RA filters. In this context, however,

TABLE VIII
HIGH POWER ANALYSIS OF THE SECOND STANDARD SINGLE-REJECT-BAND FILTER

Structure	Power of the structure (in Watts)				
Frequency	b_1	b_2	b_3	b_4	b_5
$f_1 = 3.251$ GHz	1387	23399	297582	824830	$> 10^6$
$f_2 = 3.365$ GHz	681.22	192.18	223.43	1162	27799

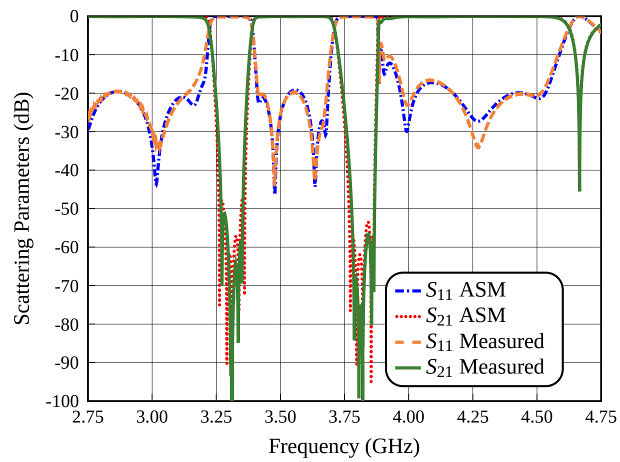

Fig. 19. Measurement of the performance of the wide dual-reject-band RA filter compared with the reverse ASM procedure.

although the power levels are indeed low, it is important to recall hat the filters discussed in this paper are used in the front-end of receivers, where the power threshold levels we have computed are indeed acceptable.

X. TECHNICAL DISCUSSION

In this section, we will discuss some of the technical aspects (or practical features) of the dual-reject-band filters based on the RAs that we discuss in this paper.

A. Reverse ASM

In order to better understand the reason for the slight disagreement between the simulations and the measurements of the wide dual-reject-band RA filter of Section VII, we have used a reverse ASM procedure. Namely, we have used the measured response as a target for the optimization of the structure in the LA space, in order to obtain an estimate of the actual dimensions of the hardware manufactured.

Fig. 19 shows the results obtained for the wide dual-reject-band RA filter response. The in-band performance of the measurement has been essentially recovered.

Analyzing now the deviations from the desired filter geometry, we note that there are errors in excess of 70 microns. With errors of this order, the measured discrepancy between measurement and simulations is indeed reasonable. This clearly demonstrates the need for a more accurate hardware manufacture procedure to get a perfect matching between simulated and experimental results.

TABLE IX
UNLOADED Q OF THE NARROW AND WIDE DUAL-BAND REJECT RA FILTERS COMPARED WITH THE STANDARD SINGLE-REJECT-BAND FILTERS

Filter Type	Freq.	Unloaded Q				
		RES_1	RES_2	RES_3	RES_4	RES_5
NDRB RA Filter	f_{LRB_1}	5547	5289	5394	5391	5479
	f_{URB_1}	5763	5896	5858	6124	5873
SRB Filter I	f_{LRB_1}	9846	10121	10044	9665	9834
SRB Filter III	f_{URB_1}	10925	10952	10930	10912	10976
WDRB RA Filter	f_{LRB_2}	5514	7459	8573	8144	6436
	f_{URB_2}	5837	9032	10281	9768	6443
SRB Filter II	f_{LRB_2}	11281	11290	11110	11378	10873
SRB Filter IV	f_{URB_2}	11403	11439	11464	11368	11405

B. Calculate Unloaded Q

Another point of interest is the achieved unloaded Q in the dual-reject-band RA filters.

Using the commercial tool CST, we have computed the unloaded Q_u of all the resonators of our dual-band filters, as well as the Q_u of reference single reject-band filters in rectangular waveguide with the same rejection bands. Table IX shows the unloaded Q values of the resonant apertures and vertical resonators of the dual-band reject RA filters compared with the ones obtained from the four standard single-reject-band filters (SRB Filter I, SRB Filter II, SRB Filter III and SRB Filter IV), where the SRB Filter I and SRB Filter II have been used for the multipaction study.

As we expected, the resonant apertures do have, in all cases, a lower unloaded Q value. However, using standard band-reject filters, we would need to double the number of filters.

XI. CONCLUSION

In this paper, we have clearly shown the feasibility of using RAs in the design of both narrow and wide dual-reject-band filters in rectangular waveguide, with good out-of-band response, and with three pass-bands between the rejection bands. Table X shows a comparison between the results we obtained and the state-of-the-art showing that our contribution is indeed unique since we are the only ones to discuss the measured results of a dual-reject-band filter in rectangular waveguide. Furthermore, yield and multipaction analyses have also been carried out. In addition to theory, the measured performance of two prototypes has also been discussed in detail indicating very good agreement with simulations, thereby fully validating the new family of filters that we propose and their systematic design procedures.

APPENDIX

As we already discussed, the parametric analysis is a necessary step in order to better understand the relation between the various structural parameters, and the performance of the basic unit cell.

In this context, therefore, the first parameter that we have changed is the width a_1 of the RA. Fig. 20 shows the effect of changing a_1 from 38.079 to 39.913 mm. As the a_1 dimension decreases, the frequency location of the first TZ goes from 3.309 to 3.423 GHz. The other dimensions of the unit cell have been optimized in order to keep fixed the location of the second TZ, and of the RZ. Table XI shows the values for the a_1, w_1 and l_1 dimensions of the structure. As we can see, even though, strictly speaking, we do not have completely independent control over the features of the structure, using optimization, it is indeed possible to move the location of the first TZ while maintaining the second TZ and the RZ at the same frequency location.

TABLE X
COMPARISON WITH THE STATE-OF-THE-ART

Ref.	Tec.	S/D	BW (MHz)	IL (dB)	Qu	Rej. (dB)
[2]	WG	S	237	1.3	-	50
[3]	WG	S	56	1.2	-	50
[17]	WG	S	2.777	0.25	5330	43
[18]	WG/PL	S	7.050	-	1430	25
[21]	WG	S	40	-	-	50
[22]	WG	S	40	-	-	50
[23]	WG	S	60	0.1	-	30
[24]	WG	S	120.75	-	-	50
[25]	WG	S	90	0.32	69	30
[26]	WG	S	120	0.1	56	20
[30]	WG	S	140	-	-	50
[31]	WG	S	290	-	-	27
[33]	WG/PL	D	588 705	- -	- -	27 26
[35]	WG/PL	S	882	0.07	-	70
[39]	WG/PL	S	680	-	-	15
[40]	WG/PL	D	318 363	0.3	175	20 20
[42]	WG	S	500	-	-	20
[43]	WG	S	200	-	-	36
[44]	WG	S	560	0.4	-	40
[45]	WG	D	53 72	< 1	5661	62.5 57.5
Our work	WG	D	95 102.5	< 1	7478	50 50

TABLE XI
PHYSICAL DIMENSIONS FOR THE UNIT CELL OF THE DUAL-REJECT-BAND FILTER, CHANGING a_1 FROM 38.079 MM TO 39.913 MM

Section Type (mm)	Resonator Dimensions (mm)	
$a_1 = 38.079$	$w_1 = 54.549$	$l_1 = 62.362$
$a_1 = 38.718$	$w_1 = 56.292$	$l_1 = 59.981$
$a_1 = 39.000$	$w_1 = 58.170$	$l_1 = 58.000$
$a_1 = 39.495$	$w_1 = 60.332$	$l_1 = 55.986$
$a_1 = 39.913$	$w_1 = 62.582$	$l_1 = 54.340$

It is important to note that a similar optimization procedure, has been followed to study the effect of changes in all other parameters discussed in this section.

The second parameter that we have changed is the height b_1 of the RA. Fig. 21 shows the effect of changing b_1 from

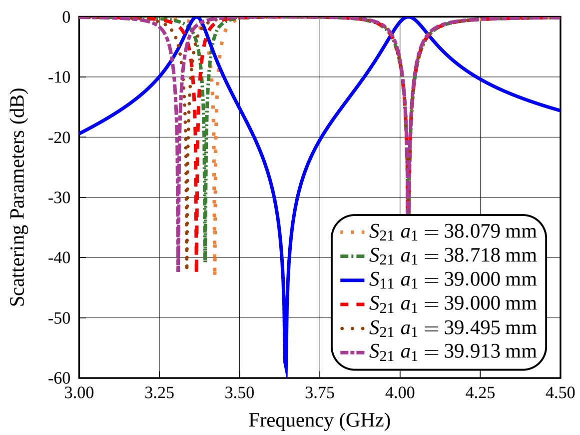

Fig. 20. Simulated performance of the UCDRB filter, changing a_1 from 38.079 to 39.913 mm.

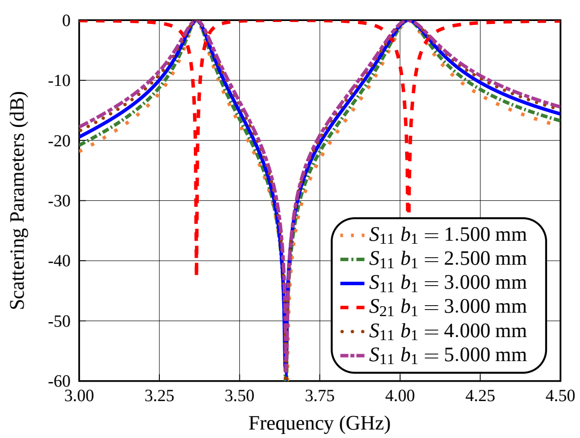

Fig. 21. Simulated performance of the UCDRB filter, changing b_1 from 1.50 to 5.0 mm.

TABLE XII
PHYSICAL DIMENSIONS FOR THE UNIT CELL OF THE DUAL-REJECT-BAND FILTER, CHANGING b_1 FROM 1.50 MM TO 5.00 MM

Section Type (mm)	Resonator Dimensions (mm)		
$b_1 = 1.500$	$a_1 = 39.465$	$w_1 = 68.538$	$l_1 = 51.264$
$b_1 = 2.000$	$a_1 = 39.275$	$w_1 = 62.665$	$l_1 = 54.386$
$b_1 = 3.000$	$a_1 = 39.000$	$w_1 = 58.170$	$l_1 = 58.000$
$b_1 = 4.000$	$a_1 = 38.883$	$w_1 = 55.988$	$l_1 = 60.349$
$b_1 = 5.000$	$a_1 = 38.776$	$w_1 = 54.787$	$l_1 = 61.868$

1.5 to 5.0 mm. As we can see, increasing the aperture height increases the bandwidth of both rejections bands. Table XII shows the values for the b_1, a_1, w_1 and l_1 dimensions of the optimized structure.

The third parameter that we have changed is the width w_1 of the resonator. Fig. 22 shows the effect of changing w_1 from 56.755 to 58.390 mm. As the w_1 dimension decreases, the frequency location of the RZ goes from 3.594 to 3.699 GHz. Table XIII shows the values for the w_1, a_1 and l_1 dimensions of the optimized structure.

The fourth parameter that we have changed is the length

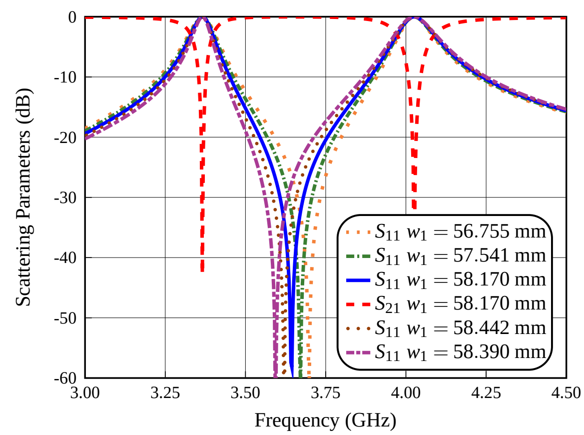

Fig. 22. Simulated performance of the UCDRB filter, changing w_1 from 56.755 to 58.390 mm.

TABLE XIII
PHYSICAL DIMENSIONS FOR THE UNIT CELL OF THE DUAL-REJECT-BAND FILTER, CHANGING w_1 FROM 56.755 MM TO 58.390 MM

Section Type (mm)	Resonator Dimensions (mm)	
$w_1 = 56.755$	$a_1 = 39.775$	$l_1 = 57.716$
$w_1 = 57.541$	$a_1 = 39.398$	$l_1 = 57.761$
$w_1 = 58.170$	$a_1 = 39.000$	$l_1 = 58.000$
$w_1 = 58.442$	$a_1 = 38.680$	$l_1 = 58.467$
$w_1 = 58.390$	$a_1 = 38.303$	$l_1 = 59.386$

l_1 of the resonator. Fig. 23 shows the effect of changing l_1 from 54.964 to 61.119 mm. As the l_1 dimension decreases, the frequency location of the second TZ goes from 3.981 to 4.074 GHz. Table XIV shows the values for l_1, a_1 and w_1 dimensions of the optimized structure.

The fifth parameter that we have changed is the height h_1 of the resonator. Fig. 24 shows the effect of changing h_1 from 20.0 to 35.0 mm. As we can see, increasing the resonator height increases the bandwidth of both rejections bands. Table XV shows the values for the h_1, b_1, a_1 and l_1

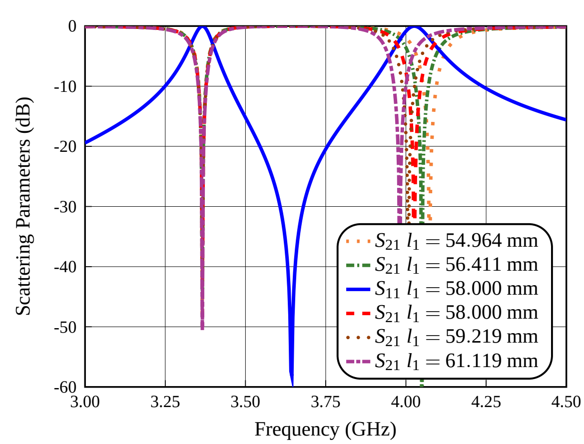

Fig. 23. Simulated performance of the UCDRB filter, changing l_1 from 54.964 to 61.119 mm.

TABLE XIV
PHYSICAL DIMENSIONS FOR THE UNIT CELL OF THE DUAL-REJECT-BAND FILTER, CHANGING l_1 FROM 54.964 TO 61.119 MM

Section Type	Resonator Dimensions (mm)	
$l_1 = 54.964$	$a_1 = 38.489$	$w_1 = 61.775$
$l_1 = 56.411$	$a_1 = 38.781$	$w_1 = 59.825$
$l_1 = 58.000$	$a_1 = 39.000$	$w_1 = 58.170$
$l_1 = 59.219$	$a_1 = 39.238$	$w_1 = 56.959$
$l_1 = 61.119$	$a_1 = 39.603$	$w_1 = 55.476$

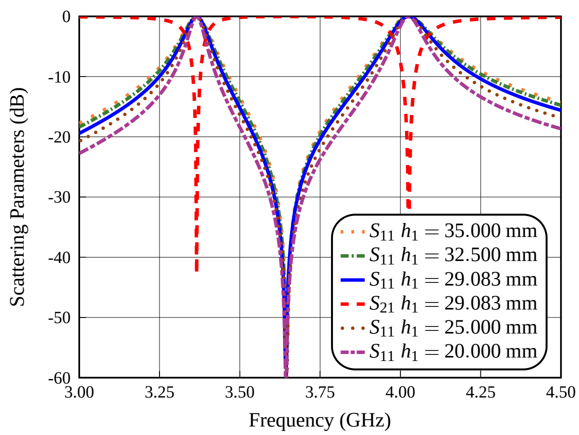

Fig. 24. Simulated performance of the UCDRB filter, changing h_1 from 20.0 to 35.0 mm.

TABLE XV
PHYSICAL DIMENSIONS FOR THE UNIT CELL OF THE DUAL-REJECT-BAND FILTER, CHANGING h_1 FROM 20.0 MM TO 35.0 MM

Section Type (mm)	Resonator Dimensions (mm)		
$h_1 = 35.000$	$b_1 = 5.000$	$a_1 = 38.454$	$l_1 = 57.833$
$h_1 = 32.500$	$b_1 = 4.062$	$a_1 = 38.653$	$l_1 = 57.882$
$h_1 = 29.083$	$b_1 = 3.000$	$a_1 = 39.000$	$l_1 = 58.000$
$h_1 = 25.000$	$b_1 = 2.080$	$a_1 = 39.451$	$l_1 = 57.944$
$h_1 = 20.000$	$b_1 = 1.305$	$a_1 = 39.806$	$l_1 = 58.050$

dimensions of the optimized structure.

Finally, the last parameter that we have studied is the thickness t_1 of the RA. Our findings indicate that, decreasing t_1 has an effect that is similar to increasing b_1. However, the effect is not as strong. As a consequence, and for the sake of space, the detailed data of the effect of t_1 have not been included.

From the results of the parametric analysis that we have just discussed, it is clearly evident that we do not have completely independent control over the three features of the basic unit cell (namely, the frequency location of TZ1, RZ, and TZ2). That is, all geometrical parameters of the structure have a direct effect on the frequency location of the three features. However, we have also shown that, using optimization, it is indeed possible to exert a limited degree of control over the performance of the unit cell.

REFERENCES

[1] R.V. Snyder, "Filter design for modern communication systems," in *2012 Asia Pacific Microw. Conf. Proc.*, 2012, pp. 673–675.

[2] R.V. Snyder, A. Mortazawi, I. Hunter, S. Bastioli, G. Macchiarella, and K. Wu, "Present and future trends in filters and multiplexers," *IEEE Trans. Microw. Theory Techn.*, vol. 63, no. 10, pp. 3324–3360, Oct. 2015.

[3] L. Young, G.L. Matthaei, and E.M.T. Jones, "Microwave band-stop filters with narrow stop bands," *IRE Trans. Microw. Theory Techn.*, vol. 10, no. 6, pp. 416–427, Nov. 1962.

[4] R. Standley and A. Todd, "A note on strip-line band-stop filters with narrow stop bands (correspondence)," *IEEE Trans. Microw. Theory Techn.*, vol. 11, no. 6, pp. 548–549, 1963.

[5] B. Schiffman and G. Matthaei, "Exact design of band-stop microwave filters," *IEEE Trans. Microw. Theory Techn.*, vol. 12, no. 1, pp. 6–15, 1964.

[6] R. Wu, S. Amari, and U. Rosenberg, "New cross-coupled microstrip band reject filters," in *2004 IEEE MTT-S Int. Microw. Symp. Dig. (IEEE Cat. No.04CH37535)*, vol. 3, 2004, pp. 1597–1600.

[7] ——, "Cross-coupled microstrip band reject filters with non-resonating nodes," *IEEE Microw. Wireless Compon. Lett.*, vol. 15, no. 9, pp. 585–587, 2005.

[8] J.-S. Hong, "Microstrip dual-mode band reject filter," in *IEEE MTT-S Int. Microw. Symp. Dig.*, 2005, pp. 945–948.

[9] T. H. Duong, J. Y. Lee, and I. S. Kim, "New bandstop filter based on capacitively coupled $\lambda/4$ short-circuited lines embedded into U.S. UWB BPF," in *2010 IEEE MTT-S Int. Microw. Symp.*, 2010, pp. 225–228.

[10] M. Attaran Kakhki and M. H. Neshati, "Experimental investigation of a dual band-reject filter using c-shaped dgs with improved q-factor," in *2010 5th Int. Symp. Telecommun.*, 2010, pp. 332–335.

[11] E. J. Naglich, J. Lee, D. Peroulis, and W. J. Chappell, "High-Q tunable bandstop filters with adaptable bandwidth and pole allocation," in *2011 IEEE MTT-S Int. Microw. Symp.*, 2011, pp. 1–4.

[12] M. Esmaeili and J. Bornemann, "Substrate integrated waveguide triple-passband dual-stopband filter using six cascaded singlets," *IEEE Microw. Wireless Compon. Lett.*, vol. 24, no. 7, pp. 439–441, 2014.

[13] L. Cui, J. Yu, S. Li, and Y. Liu, "A sharp-rejection dual-bandstop filter with multiple transmission poles and zeros based on transversal signal-interaction concepts," in *2017 IEEE 5th Int. Symp. Electromagn. Compat. (EMC-Beijing)*, 2017, pp. 1–4.

[14] Z. Jiang, Z. Sun, Y. Li, and Y. Zhao, "A wide dual band stop-band filter with two different defected microterip structures," in *2017 Prog. Electromagn. Res. Symp. - Fall (PIERS - FALL)*, 2017, pp. 1997–2000.

[15] C. Zhu, J. Xu, W. Kang, and W. Wu, "Synthesis design of microstrip triple-passband dual-stopband filter based on $\lambda/4$ uniform-impedance resonators," *IEEE Microw. Wireless Compon. Lett.*, vol. 28, no. 3, pp. 209–211, 2018.

[16] Y. Zhu and Y. Dong, "Novel dual-band bandpass-to-bandstop filter using shunt pin switches loaded on the transmission line," in *2020 IEEE/MTT-S Int. Microw. Symp. (IMS)*, 2020, pp. 924–927.

[17] J. Taub and R. Sleven, "Design of band-stop filters in the presence of dissipation," *IEEE Trans. Microw. Theory Techn.*, vol. 13, no. 5, pp. 589–616, 1965.

[18] G. Matthaei, "Magnetically tunable band-stop filters," *IEEE Trans. Microw. Theory Techn.*, vol. 13, no. 2, pp. 203–212, 1965.

[19] P. Bernardi, "A tunable absorbing band-stop filter: The field rotation filter," *IEEE Trans. Microw. Theory Techn.*, vol. 17, no. 2, pp. 62–66, 1969.

[20] R. Snyder, "Realization of dual mode band rejection filters," in *1979 IEEE MTT-S Int. Microw. Symp. Dig.*, 1979, pp. 264–268.

[21] Q. Jing-ren and Z. Wei-chen, "A new narrow dual-mode bandstop waveguide filter," in *1983 IEEE MTT-S Int. Microw. Symp. Dig.*, 1983, pp. 89–91.

[22] J.-R. Qian and W.-C. Zhuang, "New narrow-band dual-mode bandstop waveguide filters (corrections)," *IEEE Trans. Microw. Theory Techn.*, vol. 32, no. 3, pp. 324–324, 1984.

[23] J. Malherbe and J. Coetzee, "Bandstop filter in nonradiative dielectric waveguide using rectangular resonators," *IEEE Trans. Microw. Theory Techn.*, vol. 35, no. 12, pp. 1161–1163, 1987.

[24] F. Arndt and T. Sieverding, "The rigorous CAD of aperture-coupled T-junction bandstop-filters, E-plane circuit elliptic-function filters, and diplexers," in *1991 IEEE MTT-S Int. Microw. Symp. Dig.*, 1991, pp. 1103–1106 vol.3.

[25] A. Kirilenko, L. Rud, and S. Senkevich, "Spectral approach to the synthesis of bandstop filters," *IEEE Trans. Microw. Theory Techn.*, vol. 42, no. 7, pp. 1387–1392, 1994.

[26] L. Minakova and L. Rud, “Waveguide bandstop filters based on partially filled H-plane stubs,” in *14th Int. Conf. Microw, Radar and Wireless Commun. MIKON - 2002. Conf. Proc. (IEEE Cat.No.02EX562)*, vol. 1, 2002, pp. 77–80.

[27] ——, “Spectral approach to the synthesis of the waveguide bandstop filters based on dielectric rectangular posts,” in *Conf. Proc. 2000 Int. Conf. Math. Methods in Electromagn. Theory (Cat. No.00EX413)*, vol. 2, 2000, pp. 479–481.

[28] H. Uchida, H. Kamino, K. Totani, N. Yoneda, M. Miyazaki, Y. Konishi, S. Makino, J. Hirokawa, and M. Ando, “Dual-band-rejection filter for distortion reduction in RF transmitters,” in *2004 IEEE MTT-S Int. Microw. Symp. Dig. (IEEE Cat. No.04CH37535)*, vol. 2, 2004, pp. 1093–1096.

[29] ——, “Dual-band-rejection filter for distortion reduction in RF transmitters,” *IEEE Trans. Microw. Theory Techn.*, vol. 52, no. 11, pp. 2550–2556, 2004.

[30] M. Bekheit, S. Amari, W. Menzel, and U. Rosenberg, “Design of bandstop filters using cylindrical metallic posts,” in *2007 Eur. Microw. Conf.*, 2007, pp. 870–873.

[31] U. Rosenberg and S. Amari, “A novel band-reject element for pseudoelliptic bandstop filters,” *IEEE Trans. Microw. Theory Techn.*, vol. 55, no. 4, pp. 742–746, 2007.

[32] A. Kirilenko, D. Kulik, L. Mospan, and L. Rud, “Two notched band two post waveguide section,” in *2008 12th Int. Conf. Math. Methods Electromagn. Theory*, 2008, pp. 164–166.

[33] Z. Yu, L. Xu, and C. Liu, “Design of a suspended stripline dual-band band-stop filter loaded with short-ended waveguide stubs embedded in the metal housing,” *IEEE Microw. Wireless Compon. Lett.*, vol. 30, no. 11, pp. 1025–1028, 2020.

[34] A. Kirilenko and L. Mospan, “Harmonic rejection filters for the dominant and the higher waveguide modes based on the slotted strips,” in *2002 IEEE MTT-S Int. Microw. Symp. Dig. (Cat. No.02CH37278)*, vol. 1, 2002, pp. 373–376.

[35] S. A. Prikolotin and A. A. Kirilenko, “Waveguide bandstop (bandpass) filters on stepped conductors (slots) sections,” in *2011 41st Eur. Microw. Conf.*, 2011, pp. 365–368.

[36] S. Das and R. K. Gayen, “Design and analysis of slot coupled cavity for wide band band-stop filter application,” in *2012 Inter. Conf. Electromagn. Adv. Appl.*, 2012, pp. 243–246.

[37] S. Saravi, S. A. H. Gnagaraj, and M. Tayarani, “A novel composite left-right handed structure for rectangular waveguide with its multi bandstop and bandpass applications,” in *2013 21st Iranian Conf. Elect. Eng. (ICEE)*, 2013, pp. 1–5.

[38] S. Stefanovski, M. Potrebić, D. Tošić, and Z. Cvetković, “Bandstop waveguide filters with two or three rejection bands,” in *2014 29th Int. Conf. Microelectron. Proc. - MIEL 2014*, 2014, pp. 435–438.

[39] S. L. Stefanovski Pajović, M. M. Potrebić, and D. V. Tošić, “Microwave bandpass and bandstop waveguide filters using printed-circuit discontinuities,” in *2015 23rd Telecommun. Forum Telfor (TELFOR)*, 2015, pp. 520–527.

[40] M. Mrvić, M. Potrebić, and D. Tošić, “Compact E plane waveguide filter with multiple stopbands,” *Radio Sci.*, vol. 51, no. 12, pp. 1895–1904, 2016.

[41] A. Kirilenko and L. Mospan, “Bandpass and bandstop multiaperture irises for millimeter and centimeter wave range,” in *Third Int. Kharkov Symp. 'Phys. Eng. Millimeter and Submillimeter Waves'. MSMW'98. Symp.Proc. (Cat. No.98EX119)*, vol. 1, 1998, pp. 352–353.

[42] R. Cameron, M. Yu, and Y. Wang, “Direct-coupled microwave filters with single and dual stopbands,” *IEEE Trans. Microw. Theory Techn.*, vol. 53, no. 11, pp. 3288–3297, 2005.

[43] S. Amari, U. Rosenberg, and R. Wu, “In-line pseudoelliptic band-reject filters with nonresonating nodes and/or phase shifts,” *IEEE Trans. Microw. Theory Techn.*, vol. 54, no. 1, pp. 428–436, 2006.

[44] J. R. Montejo-Garai, J. A. Ruiz-Cruz, J. M. Rebollar, and T. Estrada, “In-line pure E-plane waveguide band-stop filter with wide spurious-free response,” *IEEE Microw. Wireless Compon. Lett.*, vol. 21, no. 4, pp. 209–211, 2011.

[45] J.F. Valencia Sullca, S. Cogollos, V.E. Boria, M. Guglielmi, S. Bastioli, and R.V. Snyder, “Design of dual stopband filters for interference suppression,” in *2023 IEEE MTT-S Int. Microw. Symp.*, 2023, pp. 525–528.

[46] N. Marcuvitz, *Waveguide Handbook*, ser. IEE Electromagn. Waves Series, vol. 21. Stevenage, UK: Peter Peregrinus Ltd., 1986.

[47] J.F. Valencia Sullca, S. Cogollos, V.E. Boria, and M. Guglielmi, “Compact dual-band and wideband filters with resonant apertures in rectangular waveguide,” *IEEE Trans. Microw. Theory Techn.*, vol. 70, no. 6, pp. 3125–3140, Jun. 2022.

[48] M. Guglielmi and A. A. Melcon, “Novel design procedure for microwave filters,” in *1993 23rd Eur. Microw. Conf.*, 1993, pp. 212–213.

[49] J. Bandler, R. Biernacki, S. H. Chen, R. Hemmers, and K. Madsen, “Electromagnetic optimization exploiting aggressive space mapping,” *IEEE Trans. Microw. Theory Techn.*, vol. 43, no. 12, pp. 2874–2882, Dec. 1995.

[50] G. Conciauro, M. Guglielmi, and R. Sorrentino, *Advanced Modal Analysis*. Wiley, 2000.

[51] E. Sorolla *et al.*, “An analytical model to evaluate the radiated power spectrum of a multipactor discharge in a parallel-plate region,” *IEEE Trans. Electron Devices*, vol. 55, no. 8, pp. 2252–2258, Aug. 2008.